

Polarized line formation in Multi-dimensional media-I: *Decomposition of Stokes parameters in arbitrary geometries*

L. S. Anusha¹ and K. N. Nagendra¹

¹*Indian Institute of Astrophysics, Koramangala, 2nd Block, Bangalore 560 034, India*

ABSTRACT

The solution of the polarized line radiative transfer (RT) equation in multi-dimensional geometries has been rarely addressed and only under the approximation that the changes of frequencies at each scattering are uncorrelated (complete frequency redistribution). With the increase in the resolution power of telescopes, being able to handle radiative transfer in multi-dimensional structures becomes absolutely necessary.

In the present paper, our first aim is to formulate the polarized RT equation for resonance scattering in multi-dimensional media, using the elegant technique of irreducible spherical tensors $\mathcal{T}_Q^K(i, \mathbf{\Omega})$. Our second aim is to develop a numerical method of solution based on the polarized approximate lambda iteration (PALI) approach. We consider both complete frequency redistribution (CRD) as well as partial frequency redistribution (PRD) in the line scattering.

In a multi-D geometry the radiation field is non-axisymmetrical even in the absence of a symmetry breaking mechanism such as an oriented magnetic field. We generalize here to the 3D case, the decomposition technique developed for the Hanle effect in a 1D medium which allows one to represent the Stokes parameters I, Q, U by a set of 6 cylindrically symmetrical functions. The scattering phase matrix is expressed in terms of $\mathcal{T}_Q^K(i, \mathbf{\Omega})$, ($i = 0, 1, 2, K = 0, 1, 2, -K \leq Q \leq +K$), with $\mathbf{\Omega}$, being the direction of the outgoing ray. Starting from the definition of the source vector, we show that it can be represented in terms of 6 components S_Q^K independent of $\mathbf{\Omega}$. The formal solution of the multi-dimensional transfer equation shows that the Stokes parameters can also be expanded in terms of the $\mathcal{T}_Q^K(i, \mathbf{\Omega})$. Because of the 3D-geometry, the expansion coefficients I_Q^K remain $\mathbf{\Omega}$ -dependent. We show that each I_Q^K satisfies a simple transfer equation with a source term S_Q^K and that this transfer equation provides an efficient approach for handling the polarized transfer in multi-D geometries. A PALI method for 3D, associated to a core-wing separation method for treating PRD, is developed. It is tested by comparison with 1D solutions and several benchmark solutions in the 3D case are given.

Subject headings: line: formation – radiative transfer – polarization – scattering – Sun: atmosphere

1. Introduction

The solution of the polarized line radiative transfer equation in multi-dimensional media is necessary to model the solar atmospheric features. This requirement stems from the non-axisymmetry of the radiation field arising purely due to inhomogeneous structures in the solar atmosphere. An idealization to simplify this problem, is to represent the inhomogeneities as computational cubes, characterized by their shape

and the physical parameters. This approach has proved useful in the hydrodynamics as well as the theory of radiative transfer applied to the solar atmosphere (see below). In this paper we focus on the radiative transfer aspects only. Our goal is to set up the polarized transfer equation suitable for a given geometry, and to develop numerical techniques to solve them.

Extensive work has been done in *unpolarized multi-dimensional transfer* in recent years. Here we mention only a few important developments on

this subject. A classic paper on multi-dimensional unpolarized radiative transfer is by Mihalas et al. (1978), who undertook an extensive analysis of the nature of 2D radiative transfer solutions and presented illustrative examples that helped later developments. They used a formal solver based on short characteristics but solved the problem using a second order transfer equation. A faster and more efficient formal solution based on short characteristics method for 2D was developed by Kunasz & Auer (1988). An Approximate Lambda Iteration (ALI) method for unpolarized line transfer was formulated by Auer & Paletou (1994) who used PRD in the line scattering. Auer et al. (1994) formulated an ALI method for line transfer in a 3D medium for a multi-level atom model, under the CRD approximation. Vath (1994) and Papkalla (1995) also proposed efficient 3D transfer codes based on the short characteristics formal solvers. Folini (1998) has done extensive work on the numerical techniques to solve the multi-D radiative transfer equation, and applied them to few astrophysical problems of practical interest. van Noort et al. (2002) have developed a general multi-dimensional transfer code applicable to a variety of astronomical problems. This list of papers to the unpolarized transfer in 3D does not pretend to be complete. Indeed 3D transfer techniques and applications have been the subject of keen interest in other branches of astrophysics (see e.g. Nagendra, Bonifacio & Ludwig 2009).

There are two formalisms to write the transfer equation for line polarization. The density matrix formalism (see for e.g. Landi Degl'Innocenti & Landolfi 2004, hereafter LL04), and the scattering phase matrix formalism (see e.g. Stenflo 1994). The density matrix formalism may handle polarized scattering in multi-level atoms, while it is not the case for the scattering formalism, but with the advantage that it is well adapted to handle the polarized line scattering with PRD. Again there are two streams in the scattering phase matrix formalism. The first one used the Stokes vector transfer equation (see e.g. Stenflo 1976; Dumont et al. 1977; Rees & Saliba 1982; Faurobert 1987; Nagendra 1988, 1994; Nagendra et al. 2002; Sampoorna et al. 2008a). The second stream worked with the polarized transfer equation for a reduced intensity vector (see e.g. Faurobert-Scholl 1991; Nagendra et al. 1998, 1999; Fluri et al. 2003; Sampoorna et

al. 2008b; Frisch et al. 2009; Sampoorna & Trujillo Bueno 2010).

The solution of *multi-D polarized line transfer equation* formulated in the Stokes vector basis is rather complicated to solve. The reason for this is the explicit dependence of the physical quantities on the spatial co-ordinates (X, Y, Z) , angular variables (θ, φ) and frequency x , in the standard notation. Therefore it is advantageous to write the transfer equation in a basis where it takes a simpler form. For example Chandrasekhar (1960) showed that in a one dimensional geometry, the monochromatic polarized transfer equation in the Stokes vector $(I, Q, U)^T$ basis can be transformed to a Fourier basis, where the physical quantities no longer depend on the azimuthal angle φ . A transfer equation can be written for the Fourier components of the Stokes vector and the solution is transformed back to the original $(I, Q, U)^T$ basis. This technique was later extended by Faurobert-Scholl (1991), (see also Nagendra et al. 1998) to the case of polarized line transfer in the presence of a magnetic field (Hanle effect). Frisch (2007, hereafter HF07) decomposed the Stokes vector $(I, Q, U)^T$ in terms of irreducible spherical tensors for polarimetry (see LL04 and the references cited therein). In HF07 it is shown that the Fourier expansion approach and the irreducible spherical tensor approach are somewhat equivalent, the latter being more compact and convenient to use in the scattering theory.

Dittmann (1997) formulated the solution of the polarized transfer equation for continuum scattering in 3D media. Later he proposed (Dittmann 1999) an approach of factorizing the Hanle phase matrix into a form which is suitable for the solution of the line transfer equation in 3D geometries, under the assumption of complete frequency redistribution (CRD). The Hanle line transfer equation in 2D and 3D media with CRD using the density matrix formalism was solved by Manso Sainz & Trujillo Bueno (1999). Paletou et al. (1999) solved the non-magnetic polarized resonance scattering with CRD using a perturbative approach, in a 2D geometry. Trujillo Bueno et al. (2004); Trujillo Bueno & Shchukina (2007, 2009, and references cited therein) have applied their multi-level 3D polarized transfer code to a variety of problems to understand the nature of the line transfer in the second solar spectrum. An escape proba-

bility method to compute the polarized line profiles in non-spherical winds was developed by Jeffrey (1989). In all the works mentioned above, the authors used the CRD in line scattering. Hillier (1996) solved the problem of Rayleigh scattering polarization in a 2D-spherical geometry based on the Sobolov-P approach (polarized line transfer in high speed winds) using the angle averaged partial frequency redistribution functions.

In the present paper we solve the 3D polarized line transfer equation in a non-magnetic medium under the assumption of partial frequency redistribution (PRD). For this purpose we use the traditional scattering phase matrix approach. We follow the decomposition technique of HF07 all through the present paper. Basically we start from the decomposition of Stokes parameters in terms of the irreducible spherical tensors for 1D media, developed by HF07, and extend it to handle the case of transfer in multi-dimensional media. For the PRD we consider the collisional redistribution matrix (Domke & Hubeny 1988; Bommier 1997) for a 2-level atom model with unpolarized ground level.

A polarized RT equation in Stokes vector formalism is presented in § 2. A general multipolar expansion of the Stokes source vector and Stokes parameters in terms of the irreducible spherical tensors and the corresponding RT equation is presented in § 3. For the formal solution of the transfer equation we use the finite volume element method formulated by Adam (1990), extended here to include polarization and PRD. We briefly explain in § 4 the numerical method that we have developed in the present paper. Details of the numerical method are presented in Appendix B. In § 5 we present some solutions to understand the nature of polarization in a 3D scattering medium. They may serve as benchmarks for further exploration. In § 6 we present our conclusions.

2. Polarized radiative transfer in a 3D medium – Stokes vector basis

The transfer equation in divergence form in the atmospheric reference frame (see Figure 2) is writ-

ten as

$$\begin{aligned} \boldsymbol{\Omega} \cdot \nabla \mathbf{I}(\mathbf{r}, \boldsymbol{\Omega}, x) = \\ -[\kappa_l(\mathbf{r})\phi(x) + \kappa_c(\mathbf{r})][\mathbf{I}(\mathbf{r}, \boldsymbol{\Omega}, x) - \mathbf{S}(\mathbf{r}, \boldsymbol{\Omega}, x)], \end{aligned} \quad (1)$$

where $\mathbf{I} = (I, Q, U)^T$ is the Stokes vector, with I , Q and U the Stokes parameters defined below. Following Chandrasekhar (1960), we consider an elliptically polarized beam of light, the vibrations of the electric vector of which describe an ellipse. If I_l and I_r denote the components of the specific intensity of this beam of light along two mutually perpendicular directions l and r , in a plane transverse to the propagation direction, then we define

$$\begin{aligned} I &= I_l + I_r, \\ Q &= I_l - I_r, \\ U &= (I_l - I_r) \tan 2\chi, \end{aligned} \quad (2)$$

where χ is the angle between the direction l and the semi major axis of the ellipse. Positive value of Q is defined to be in a direction perpendicular to the surface, and negative Q in the directions parallel to it. The quantity $\mathbf{r} = (X, Y, Z)$ is the position vector of the ray in the Cartesian co-ordinate system. The unit vector $\boldsymbol{\Omega} = (n_X, n_Y, n_Z) = (\sin \theta \cos \varphi, \sin \theta \sin \varphi, \cos \theta)$ describes the direction cosines of the ray in the atmosphere with respect to the atmospheric normal, with θ, φ being polar and azimuthal angles of the ray. The quantity κ_l is the frequency averaged line opacity, ϕ is the Voigt profile function and κ_c is the continuum opacity. Frequency is measured in reduced units, namely $x = (\nu - \nu_0)/\Delta\nu_D$, where $\Delta\nu_D$ is the Doppler width. The total source vector \mathbf{S} is given by

$$\mathbf{S}(\mathbf{r}, \boldsymbol{\Omega}, x) = \frac{\kappa_l(\mathbf{r})\phi(x)\mathbf{S}_l(\mathbf{r}, \boldsymbol{\Omega}, x) + \kappa_c(\mathbf{r})\mathbf{S}_c(\mathbf{r}, x)}{\kappa_l(\mathbf{r})\phi(x) + \kappa_c(\mathbf{r})}. \quad (3)$$

Here \mathbf{S}_c is the continuum source vector namely $(B(\mathbf{r}), 0, 0)^T$ with $B(\mathbf{r})$ being the Planck function at the line center frequency. The line source vector can be expressed as

$$\begin{aligned} \mathbf{S}_l(\mathbf{r}, \boldsymbol{\Omega}, x) &= \mathbf{G}(\mathbf{r}) + \int_{-\infty}^{+\infty} dx' \\ &\times \oint \frac{d\boldsymbol{\Omega}'}{4\pi} \frac{\hat{R}(x, x', \boldsymbol{\Omega}, \boldsymbol{\Omega}')}{\phi(x')} \mathbf{I}(\mathbf{r}, \boldsymbol{\Omega}', x'), \end{aligned} \quad (4)$$

where $\mathbf{G} = (\epsilon B(\mathbf{r}), 0, 0)^T$ is the thermal source. $\epsilon = \Gamma_I/(\Gamma_R + \Gamma_I)$ with Γ_I and Γ_R being the inelastic collision rate and the radiative de-excitation rate respectively, so that ϵ is the rate of destruction by inelastic collisions, also known as the thermalization parameter. The damping parameter is computed using $a = a_R[1 + (\Gamma_E + \Gamma_I)/\Gamma_R]$ where $a_R = \Gamma_R/4\pi\Delta\nu_D$ and Γ_E is the elastic collision rate. \hat{R} is the redistribution matrix. The solid angle element $d\Omega' = \sin\theta' d\theta' d\varphi'$ $\theta \in [0, \pi]$ and $\varphi \in [0, 2\pi]$. To construct the decomposition in multipolar components, it is convenient to work with the transfer equation written along a ray path. It has the form

$$\frac{d\mathbf{I}(\mathbf{r}, \boldsymbol{\Omega}, x)}{ds} = -\kappa_{tot}(\mathbf{r}, x)[\mathbf{I}(\mathbf{r}, \boldsymbol{\Omega}, x) - \mathbf{S}(\mathbf{r}, \boldsymbol{\Omega}, x)], \quad (5)$$

where s is the path length along the ray (see Figure 1) and $\kappa_{tot}(\mathbf{r}, x)$ is the total opacity given by

$$\kappa_{tot}(\mathbf{r}, x) = \kappa_l(\mathbf{r})\phi(x) + \kappa_c(\mathbf{r}). \quad (6)$$

The formal solution of Equation (5) is given by

$$\begin{aligned} \mathbf{I}(\mathbf{r}, \boldsymbol{\Omega}, x) &= \mathbf{I}(\mathbf{r}_0, \boldsymbol{\Omega}, x) e^{-\int_{s_0}^s \kappa_{tot}(\mathbf{r} - s''\boldsymbol{\Omega}, x) ds''} \\ &+ \int_{s_0}^s \mathbf{S}(\mathbf{r} - s'\boldsymbol{\Omega}, \boldsymbol{\Omega}, x) e^{-\int_{s'}^s \kappa_{tot}(\mathbf{r} - s''\boldsymbol{\Omega}, x) ds''} \\ &\times [\kappa_{tot}(\mathbf{r} - s'\boldsymbol{\Omega}, x)] ds'. \end{aligned} \quad (7)$$

$\mathbf{I}(\mathbf{r}_0, \boldsymbol{\Omega}, x)$ is the boundary condition imposed at $\mathbf{r}_0 = (X_0, Y_0, Z_0)$.

3. Decomposition of Stokes vectors for multi-dimensional radiative transfer

In this section we show how to generalize to a multi-D geometry the Stokes parameters decomposition method developed for the Hanle effect in 1D geometry.

3.1. A multipolar expansion of the Stokes source vector and the Stokes intensity vector in a 3D medium

We derive the required decomposition starting from the polarized transfer equation in $(I, Q, U)^T$ basis. For simplicity, we assume that the redistribution matrix can be written as a product of angle-averaged redistribution functions and an explicit

angle (θ, φ) dependent phase matrix. The scattering phase matrix can be expressed in terms of the irreducible spherical tensors introduced in LL04. The ij -th element of the redistribution matrix in the atmospheric reference frame (Bommier 1997) is given by

$$\begin{aligned} R_{ij}(x, x', \boldsymbol{\Omega}, \boldsymbol{\Omega}') &= \\ \sum_{KQ} W_K \mathcal{T}_Q^K(i, \boldsymbol{\Omega}) (-1)^Q \mathcal{T}_{-Q}^K(j, \boldsymbol{\Omega}') R^K(x, x'), \end{aligned} \quad (8)$$

where $(i, j) = (1, 2, 3)$ and

$$R^K(x, x') = W_K \{ \alpha R_{II}(x, x') + [\beta^{(K)} - \alpha] R_{III}(x, x') \}. \quad (9)$$

In the present paper, we consider only the linear polarization. Therefore, $K = 0, 2$ and $Q \in [-K, +K]$. The weights W_K depend on the line under consideration (see LL04). Here $R_{II}(x, x')$ and $R_{III}(x, x')$ are the angle-averaged versions of redistribution functions (see Hummer 1962). The branching ratios are given by

$$\alpha = \frac{\Gamma_R}{\Gamma_R + \Gamma_E + \Gamma_I}, \quad (10)$$

$$\beta^{(K)} = \frac{\Gamma_R}{\Gamma_R + D^{(K)} + \Gamma_I}, \quad (11)$$

with $D^{(0)} = 0$ and $D^{(2)} = c\Gamma_E$, where c is a constant, taken to be 0.379 (see Faurobert-Scholl 1992). Substituting Equations (8) and (9) in Equation (4), we can write the i -th component of the line source vector as

$$\begin{aligned} S_{i,l}(\mathbf{r}, \boldsymbol{\Omega}, x) &= G_i(\mathbf{r}) + \frac{1}{\phi(x)} \int_{-\infty}^{+\infty} dx' \oint \frac{d\Omega'}{4\pi} \\ &\times \sum_{j=0}^3 \sum_{KQ} \mathcal{T}_Q^K(i, \boldsymbol{\Omega}) (-1)^Q \mathcal{T}_{-Q}^K(j, \boldsymbol{\Omega}') \\ &\times R^K(x, x') I_j(\mathbf{r}, \boldsymbol{\Omega}', x'). \end{aligned} \quad (12)$$

Denoting $G_Q^K = \delta_{K0} \delta_{Q0} G(\mathbf{r})$, where $G(\mathbf{r}) = \epsilon B(\mathbf{r})$ we can write the i -th component of the thermal source vector as

$$G_i(\mathbf{r}) = \sum_{KQ} \mathcal{T}_Q^K(i, \boldsymbol{\Omega}) G_Q^K(\mathbf{r}). \quad (13)$$

Substituting Equation (13) in Equation (12) we can write the line source vector as

$$S_{i,l}(\mathbf{r}, \boldsymbol{\Omega}, x) = \sum_{KQ} \mathcal{T}_Q^K(i, \boldsymbol{\Omega}) S_{Q,l}^K(\mathbf{r}, x), \quad (14)$$

where

$$S_{Q,l}^K(\mathbf{r}, x) = G_Q^K(\mathbf{r}) + \frac{1}{\phi(x)} \int_{-\infty}^{+\infty} dx' \oint \frac{d\boldsymbol{\Omega}'}{4\pi} \\ \times R^K(x, x') \sum_{j=0}^3 (-1)^Q \mathcal{T}_{-Q}^K(j, \boldsymbol{\Omega}') I_j(\mathbf{r}, \boldsymbol{\Omega}', x'). \quad (15)$$

Notice that the components $S_{Q,l}^K(\mathbf{r}, x)$ now depend only on the spatial variables (X, Y, Z) and frequency x . The (θ, φ) dependence is fully contained in $\mathcal{T}_Q^K(i, \boldsymbol{\Omega})$. These quantities are listed in LL04 (chapter 5, Table 5.6, p. 211, see also Table 2 of HF07). We can define the monochromatic optical depth scale as

$$\tau_x(X, Y, Z) = \int_{s_0}^s \kappa_{tot}(\mathbf{r} - s''\boldsymbol{\Omega}, x) ds'', \quad (16)$$

where τ_x is measured along a given ray determined by the direction $\boldsymbol{\Omega}$. We use the notation τ_X , τ_Y and τ_Z to denote the optical depths along the X , Y and Z axes respectively at line center. Substituting Equation (14) in Equation (7), the components of \mathbf{I} can be written as

$$I_i(\mathbf{r}, \boldsymbol{\Omega}, x) = \sum_{KQ} \mathcal{T}_Q^K(i, \boldsymbol{\Omega}) I_Q^K(\mathbf{r}, \boldsymbol{\Omega}, x), \quad (17)$$

where

$$I_Q^K(\mathbf{r}, \boldsymbol{\Omega}, x) = I_{Q,0}^K(\mathbf{r}_0, \boldsymbol{\Omega}, x) e^{-\int_{s_0}^s \kappa_{tot}(\mathbf{r} - s''\boldsymbol{\Omega}, x) ds''} \\ + \int_{s_0}^s e^{-\int_{s'}^s \kappa_{tot}(\mathbf{r} - s''\boldsymbol{\Omega}, x) ds''} \left[p_x S_{Q,l}^K(\mathbf{r} - s'\boldsymbol{\Omega}, x) \right. \\ \left. + (1 - p_x) S_{Q,C}^K(\mathbf{r} - s'\boldsymbol{\Omega}, x) \right] [\kappa_{tot}(\mathbf{r} - s'\boldsymbol{\Omega}, x)] ds'. \quad (18)$$

$I_{Q,0}^K = I_0(\mathbf{r}_0, \boldsymbol{\Omega}, x) \delta_{K0} \delta_{Q0}$ are the intensity components at the lower boundary. The quantities $S_{Q,C}^K = S_C(\mathbf{r}, x) \delta_{K0} \delta_{Q0}$ denote the continuum source vector components. We assume that $S_C(\mathbf{r}, x) = B(\mathbf{r})$. The ratio of the line opacity to the total opacity is given by

$$p_x = \kappa_l(\mathbf{r}) \phi(x) / \kappa_{tot}(\mathbf{r}, x). \quad (19)$$

Expressed in terms of optical depth along the ray, Equation (18) can be written as

$$I_Q^K(\mathbf{r}, \boldsymbol{\Omega}, x) = I_{Q,0}^K(\mathbf{r}_0, \boldsymbol{\Omega}, x) e^{-\tau_{x,max}} \\ + \int_0^{\tau_{x,max}} e^{-\tau'_x(\mathbf{r}')} \left[p_x S_{Q,l}^K(\mathbf{r}', x) \right. \\ \left. + (1 - p_x) S_{Q,C}^K(\mathbf{r}', x) \right] d\tau'_x(\mathbf{r}'). \quad (20)$$

In Equation (20) $\tau_{x,max}$ is the maximum optical depth when measured along the ray. Let $S_Q^K = p_x S_{Q,l}^K + (1 - p_x) S_{Q,C}^K$. Using the expansions in Equations (14) and (17), it can be shown that S_Q^K and I_Q^K satisfy a transfer equation of the form

$$-\frac{1}{\kappa_{tot}(\mathbf{r}, x)} \boldsymbol{\Omega} \cdot \nabla I_Q^K(\mathbf{r}, \boldsymbol{\Omega}, x) = \\ [I_Q^K(\mathbf{r}, \boldsymbol{\Omega}, x) - S_Q^K(\mathbf{r}, x)]. \quad (21)$$

The great advantage of working with the irreducible intensity components I_Q^K is that the corresponding source terms S_Q^K become independent of the direction $\boldsymbol{\Omega}$ of the ray.

Substituting Equation (17) in Equation (15) we obtain

$$S_{Q,l}^K(\mathbf{r}, x) = G_Q^K(\mathbf{r}) + \bar{J}_Q^K(\mathbf{r}, x), \quad (22)$$

where

$$\bar{J}_Q^K(\mathbf{r}, x) = \frac{1}{\phi(x)} \int_{-\infty}^{+\infty} dx' \oint \frac{d\boldsymbol{\Omega}'}{4\pi} R^K(x, x') \\ \times \sum_{j=0}^3 \sum_{K'Q'} (\mathcal{T}_Q^K)^*(j, \boldsymbol{\Omega}') \mathcal{T}_{Q'}^{K'}(j, \boldsymbol{\Omega}') I_{Q'}^{K'}(\mathbf{r}, \boldsymbol{\Omega}', x'). \quad (23)$$

The symbol $*$ represents the conjugation. \mathcal{T}_Q^K satisfy the conjugation property

$$(\mathcal{T}_Q^K)^*(j, \boldsymbol{\Omega}) = (-1)^Q \mathcal{T}_{-Q}^K(j, \boldsymbol{\Omega}). \quad (24)$$

Equation (23) can be expressed in a matrix form as

$$\bar{\mathcal{J}}(\mathbf{r}, x) = \frac{1}{\phi(x)} \int_{-\infty}^{+\infty} dx' \oint \frac{d\boldsymbol{\Omega}'}{4\pi} \\ \hat{R}(x, x') \hat{\Psi}(\boldsymbol{\Omega}') \mathcal{I}(\mathbf{r}, \boldsymbol{\Omega}', x'), \quad (25)$$

where the components of the vectors $\bar{\mathcal{J}}$ and \mathcal{I} are \bar{J}_Q^K and I_Q^K respectively. The matrix \hat{R} is given by

$$\hat{R}(x, x') = \hat{W}[\hat{\alpha} R_{II}(x, x') + (\hat{\beta} - \hat{\alpha}) R_{III}(x, x')], \quad (26)$$

where

$$\hat{W} = \text{diag}\{W_0, W_2, W_2, W_2, W_2, W_2\}, \quad (27)$$

$$\hat{\alpha} = \text{diag}\{\alpha, \alpha, \alpha, \alpha, \alpha, \alpha\}, \quad (28)$$

$$\hat{\beta} = \text{diag}\{\beta^{(0)}, \beta^{(2)}, \beta^{(2)}, \beta^{(2)}, \beta^{(2)}, \beta^{(2)}\}. \quad (29)$$

The elements of the matrix $\hat{\Psi}(\boldsymbol{\Omega})$ are

$$\Psi_{QQ'}^{KK'}(\boldsymbol{\Omega}) = \sum_{j=0}^3 (\mathcal{T}_Q^K)^*(j, \boldsymbol{\Omega}) \mathcal{T}_{Q'}^{K'}(j, \boldsymbol{\Omega}). \quad (30)$$

$\Psi_{QQ'}^{KK'}$ are exactly the same as $\Gamma_{KK', QQ'}(\boldsymbol{\Omega})$ given in LL04 (Appendix A.20). We stress here that the phase matrix $\hat{\Psi}(\boldsymbol{\Omega}')$ in Equation (25) depends only on the directions $\boldsymbol{\Omega}'$ of the incident rays. The dependence on $\boldsymbol{\Omega}$, present in the phase matrix when one works with the (I, Q, U) basis, disappears when the polarized radiation field is represented with the six I_Q^K components. For short we refer to this representation as the ‘‘reduced basis’’. The matrix $\hat{\Psi}(\boldsymbol{\Omega}')$ differs from the $\hat{\Psi}(\mu')$ matrix that appears in 1D radiative transfer problems (see HF07, Nagendra et al. 1998), since it now depends on the azimuthal angle φ' of the incident ray.

3.2. Polarized Radiative transfer equation for the real irreducible intensity vector in a 3D medium

The irreducible components I_Q^K and S_Q^K and the phase matrix elements $\Psi_{QQ'}^{KK'}$ introduced in § 3.1 are complex quantities. For practical computations, we prefer working with the real quantities. In this section we transform those quantities into the real space. For this purpose we follow the procedure given in HF07. We define

$$\begin{aligned} I_Q^{K,x}(\mathbf{r}, \boldsymbol{\Omega}, x) &= \text{Re}\{I_Q^K(\mathbf{r}, \boldsymbol{\Omega}, x)\}, \\ I_Q^{K,y}(\mathbf{r}, \boldsymbol{\Omega}, x) &= \text{Im}\{I_Q^K(\mathbf{r}, \boldsymbol{\Omega}, x)\}. \end{aligned} \quad (31)$$

It can be shown that $\mathcal{I}^r = (I_0^0, I_0^2, I_1^{2,x}, I_1^{2,y}, I_2^{2,x}, I_2^{2,y})^T$ and the corresponding source vector \mathcal{S}^r satisfy a transfer equation of the form

$$\begin{aligned} -\frac{1}{\kappa_{tot}(\mathbf{r}, x)} \boldsymbol{\Omega} \cdot \nabla \mathcal{I}^r(\mathbf{r}, \boldsymbol{\Omega}, x) = \\ [\mathcal{I}^r(\mathbf{r}, \boldsymbol{\Omega}, x) - \mathcal{S}^r(\mathbf{r}, x)], \end{aligned} \quad (32)$$

where $\mathcal{S}^r(\mathbf{r}, x) = p_x \mathcal{S}_I^r(\mathbf{r}, x) + (1 - p_x) \mathcal{S}_C^r(\mathbf{r}, x)$ with

$$\begin{aligned} \mathcal{S}_I^r(\mathbf{r}, x) &= \epsilon \mathbf{B}(\mathbf{r}) + \frac{1}{\phi(x)} \int_{-\infty}^{+\infty} dx' \\ &\times \oint \frac{d\boldsymbol{\Omega}'}{4\pi} \hat{R}(x, x') \hat{\Psi}^r(\boldsymbol{\Omega}') \mathcal{I}^r(\mathbf{r}, \boldsymbol{\Omega}', x'). \end{aligned} \quad (33)$$

In the above equation, the real part of the scattering phase matrix $\hat{\Psi}^r(\boldsymbol{\Omega})$ has the form

$$\hat{\Psi}^r(\boldsymbol{\Omega}) = \hat{T}^{-1} \hat{\Psi}(\boldsymbol{\Omega}) \hat{T}, \quad (34)$$

where the matrix \hat{T} is given by

$$\hat{T} = \begin{pmatrix} 1 & 0 & 0 & 0 & 0 & 0 \\ 0 & 1 & 0 & 0 & 0 & 0 \\ 0 & 0 & 1 & i & 0 & 0 \\ 0 & 0 & -1 & i & 0 & 0 \\ 0 & 0 & 0 & 0 & 1 & i \\ 0 & 0 & 0 & 0 & 1 & -i \end{pmatrix}. \quad (35)$$

The elements of the scattering phase matrix $\hat{\Psi}^r(\boldsymbol{\Omega})$ are given in the Appendix A. The matrix $\hat{\Psi}^r(\boldsymbol{\Omega})$ has only 21 distinct coefficients due to symmetry reasons. We remark that $\hat{\Psi}^r(\boldsymbol{\Omega})$ is a full matrix to be used in Multi-D case, unlike the $\hat{\Psi}(\mu)$ that is used in the 1-D case, which has a sparse structure. After solving the transfer problem in the real, reduced basis, one has to transform back to the Stokes $(I, Q, U)^T$ basis. This can be done using the following equations (see also Appendix B of HF07).

$$\begin{aligned} I(\mathbf{r}, \boldsymbol{\Omega}, x) &= I_0^0 + \frac{1}{2\sqrt{2}} (3 \cos^2 \theta - 1) I_0^2 \\ &- \sqrt{3} \cos \theta \sin \theta (I_1^{2,x} \cos \varphi - I_1^{2,y} \sin \varphi) \\ &+ \frac{\sqrt{3}}{2} (1 - \cos^2 \theta) (I_2^{2,x} \cos 2\varphi - I_2^{2,y} \sin 2\varphi), \end{aligned} \quad (36)$$

$$\begin{aligned} Q(\mathbf{r}, \boldsymbol{\Omega}, x) &= -\frac{3}{2\sqrt{2}} (1 - \cos^2 \theta) I_0^2 \\ &- \sqrt{3} \cos \theta \sin \theta (I_1^{2,x} \cos \varphi - I_1^{2,y} \sin \varphi) \\ &- \frac{\sqrt{3}}{2} (1 + \cos^2 \theta) (I_2^{2,x} \cos 2\varphi - I_2^{2,y} \sin 2\varphi), \end{aligned} \quad (37)$$

$$\begin{aligned} U(\mathbf{r}, \boldsymbol{\Omega}, x) &= \sqrt{3} \sin \theta (I_1^{2,x} \sin \varphi + I_1^{2,y} \cos \varphi) \\ &+ \sqrt{3} \cos \theta (I_2^{2,x} \sin 2\varphi + I_2^{2,y} \cos 2\varphi). \end{aligned} \quad (38)$$

The irreducible components in the above equations also depend on \mathbf{r} , $\boldsymbol{\Omega}$ and x .

4. The Numerical Method of Solution

For the numerical solution of the 3D transfer problem (Equation (32)), we use a polarized approximate lambda iteration (PALI) method, associated to a core-wing separation method to handle PRD. The 6 component scattering integral can be expressed as

$$\overline{\mathcal{J}}^r(\mathbf{r}, x) = \int_{-\infty}^{+\infty} dx' \frac{\hat{R}(x, x')}{\phi(x)} \mathcal{J}^r(\mathbf{r}, x'), \quad (39)$$

with

$$\mathcal{J}^r(\mathbf{r}, x) = \oint \frac{d\boldsymbol{\Omega}'}{4\pi} \hat{\Psi}(\boldsymbol{\Omega}') \mathcal{I}(\mathbf{r}, \boldsymbol{\Omega}', x). \quad (40)$$

The formal solution for $\mathcal{I}(\mathbf{r}, \boldsymbol{\Omega}', x)$ allows us to define the operator $\hat{\Lambda}_x$ as

$$\mathcal{J}^r(\mathbf{r}, x) = \hat{\Lambda}_x[\mathcal{S}^r(\mathbf{r}, x)]. \quad (41)$$

Applying the operator splitting technique, the scattering integral at the $(n+1)$ -th iteration can be written as

$$\begin{aligned} \overline{\mathcal{J}}^{r,n+1}(\mathbf{r}, x) &= \int_{-\infty}^{+\infty} dx' \frac{\hat{R}(x, x')}{\phi(x)} \\ &[\hat{\Lambda}_{x'}^* + (\hat{\Lambda}_{x'} - \hat{\Lambda}_{x'}^*)] \mathcal{S}^{r,n+1}(\mathbf{r}, x'). \end{aligned} \quad (42)$$

We can re-write the scattering integral as

$$\begin{aligned} \overline{\mathcal{J}}^{r,n+1}(\mathbf{r}, x) &= \overline{\mathcal{J}}^{r,n}(\mathbf{r}, x) + \int_{-\infty}^{+\infty} dx' \\ &\frac{\hat{R}(x, x')}{\phi(x)} \hat{\Lambda}_{x'}^* p_{x'} \delta \mathcal{S}_l^{r,n}(\mathbf{r}, x'). \end{aligned} \quad (43)$$

It is useful to notice here that $\delta \mathcal{S}_l^{r,n}(\mathbf{r}, x) = p_x \delta \mathcal{S}_l^{r,n}(\mathbf{r}, x)$. The correction to the line source vector in the n -th iteration is given by

$$\begin{aligned} \delta \mathcal{S}_l^{r,n}(\mathbf{r}, x) &= \\ \overline{\mathcal{J}}^{r,n+1}(\mathbf{r}, x) + \epsilon \mathbf{B}(\mathbf{r}) - \mathcal{S}_l^{r,n}. \end{aligned} \quad (44)$$

Further details of the numerical method of solution to solve the 3D transfer equation is given in Appendix B.

4.1. The formal solution in 3D geometry

In this section we generalize the method of Adam (1990) for 3D transfer to include the polarization and PRD. For the sake of brevity we drop the explicit dependence of the physical quantities on the arguments. To start with, we divide the computational domain (a cube) in to a 3 dimensional mesh of grid points (X_i, Y_j, Z_k) with $i = 1, 2, \dots, N_X; j = 1, 2, \dots, N_Y; k = 1, 2, \dots, N_Z$. A discretization of Equation (32) on this mesh can be written as

$$\begin{aligned} &-\frac{1}{\kappa_{tot}} \left[n_X \frac{\mathcal{I}_{ijk}^r - \mathcal{I}_{i-a,j,k}^r}{X_i - X_{i-a}} \right. \\ &+ n_Y \frac{\mathcal{I}_{ijk}^r - \mathcal{I}_{i,j-b,k}^r}{Y_j - Y_{j-b}} + n_Z \frac{\mathcal{I}_{ijk}^r - \mathcal{I}_{i,j,k-c}^r}{Z_k - Z_{k-c}} \left. \right] \\ &= [\mathcal{I}_{ijk}^r - \mathcal{S}_{ijk}^r], \end{aligned} \quad (45)$$

where a, b, c are the increments, taking values $+1$ or -1 depending on the choice of the direction vector $\boldsymbol{\Omega}$. In deriving Equation (45) we have used a finite difference method where the differential operator is represented to the linear order. Equation (45) can be simplified to get

$$\begin{aligned} \mathcal{I}_{ijk}^r &= \left\{ \mathcal{S}_{ijk}^r + \frac{1}{\kappa_{tot}} \left[n_X \frac{\mathcal{I}_{i-a,j,k}^r}{X_i - X_{i-a}} \right. \right. \\ &+ n_Y \frac{\mathcal{I}_{i,j-b,k}^r}{Y_j - Y_{j-b}} + n_Z \frac{\mathcal{I}_{i,j,k-c}^r}{Z_k - Z_{k-c}} \left. \left. \right] \right\} / \\ &\left\{ 1 + \frac{1}{\kappa_{tot}} \left(\frac{n_X}{X_i - X_{i-a}} + \frac{n_Y}{Y_j - Y_{j-b}} + \frac{n_Z}{Z_k - Z_{k-c}} \right) \right\}. \end{aligned} \quad (46)$$

Equation (46) is solved recursively, namely the intensity at any spatial point (ijk) depends only on the intensity at 3 previous neighboring points $(i-a, j, k), (i, j-b, k), (i, j, k-c)$.

It is shown by Adam (1990) that this numerical approach is unconditionally stable. The linear differencing is relatively less accurate compared to the short characteristic method, as a formal solver. However, we can overcome this problem of accuracy by taking sufficiently small step sizes in the (X, Y, Z) co-ordinates. The main emphasis of the present paper is to understand the nature of 3D solutions for the problem at hand, instead of devising highly accurate and rapid methods. These

issues would be addressed in another paper. In § 5 we present few benchmark solutions computed by the method presented in Appendix B.

Computational details: We consider a self-emitting cube (or a slab) for the results presented in this paper. A Gaussian angle grid of 6 inclination ($\theta=83.5^\circ, 60^\circ, 27.4^\circ, 96.5^\circ, 120^\circ, 152.6^\circ$) and 8 azimuths ($\varphi=7^\circ, 36^\circ, 85^\circ, 146^\circ, 213^\circ, 274^\circ, 323^\circ, 352^\circ$) are used. We have numerically tested that this kind of angular resolution is quite reasonable and gives stable solutions. A spatial grid resolution of 15 points per decade or 20 points per decade in X , Y and Z directions are used. The spatial grid is logarithmic, with fine gridding near the boundaries. A logarithmic frequency grid of 31 points covering 20 Doppler widths ($0 \leq x \leq x_{\max} = 20$) is sufficient for the examples shown in this paper. The standard model parameters are listed in § 5.1. The specific model parameters for each Figure are given in the Figures and the respective Figure captions.

5. Results and Discussions

In this section we present sample results to show the correctness of the Stokes decomposition procedure, as applied to the 3D case. Further we show some results to validate the numerical method that computes the 3D solution. The departure of the radiation field from axis-symmetry is discussed in some detail. A study of the PRD effects in 3D media is also presented along with the role of collisional redistribution.

5.1. A validation test for the 3D polarized radiative transfer solution

It is possible to test the correctness of a 3D solution by going to a geometric situation where the 3D cube mimics an 1D slab. For $T_X \gg T_Z$ and $T_Y \gg T_Z$, with a finite value of $T_Z = T$, the computational box looks like a planar slab of optical thickness T . We can expect the emergent solution $(I, Q/I, U/I)^T$ at the center of the upper surface ($T_X/2, T_Y/2, \tau_Z = 0$) of such a cube to approach the emergent 1D solution $(I, Q/I, U/I)^T$ at $\tau_Z = 0$. Figure 3 presents this validation test. The 1D benchmark solution is computed using a PALI method (see e.g. Nagendra et al. 1999; Fluri et al. 2003). The model parameters are $T_X = T_Y = 10^7$, and $T_Z = T = 10$; the

elastic and inelastic collision rates are respectively $\Gamma_E/\Gamma_R = 10^{-4}$, $\Gamma_I/\Gamma_R = 10^{-4}$. The damping parameter of the Voigt profile is $a = 2 \times 10^{-3}$. The branching ratios for this choice of model parameters are $(\alpha, \beta^{(0)}, \beta^{(2)}) \approx (1, 1, 1)$ (see the exact values in Table 2). We consider the pure line case ($\kappa_c = 0$), and scattering according to PRD (see Equation (8)). The internal thermal sources are taken as constant (the Planck function $B = 1$). The medium is assumed to be self-emitting (no incident radiation on the boundaries). The emergent $(I, Q/I, U/I)$ profiles are shown for a choice of angles $(\mu, \varphi)=(0.11, 7^\circ)$. From Figures 3(a) and 3(b), we see that there is a good agreement between the two solutions. In the planar case $U/I \equiv 0$. The U/I in the 3D case approaches this value to a high accuracy (10^{-5} percent). This figure shows the correctness of the Stokes decomposition expressions, and also the numerical method that computes the 3D solution.

5.2. The nature of irreducible intensity components \mathcal{I}^r in a 3D medium

In § 3 we showed how to express the Stokes parameters in terms of the irreducible intensity components. These components are more fundamental than the Stokes parameters themselves. Their study is useful to understand the behavior of Stokes parameters - which are actually the measurable quantities. If we choose optical thickness in the X , Y , and Z directions as $T_X = T_Y = T_Z = T$, then we encounter a situation where the 3D nature of the transfer problem is clearly exhibited. Figure 4 shows the spatially averaged emergent \mathcal{I}^r at the top surface ($\tau_Z = 0$). We prefer to show the surface averaged \mathcal{I}^r because the components themselves sensitively depend on the spatial location on the surface. It is useful to note that the spatially averaged \mathcal{I}^r retain the original symmetries even after averaging. The results are shown for $\mu = 0.11$ and for all the 8 values of the azimuth angle φ (namely $7^\circ, 36^\circ, 85^\circ, 146^\circ, 213^\circ, 274^\circ, 323^\circ, 352^\circ$). The model parameters and the physical conditions chosen for Figure 4 are the same as in Figure 3, except for $T_X=T_Y=T_Z=T=100$.

The I_0^0 component is the driving term. It is also the largest in magnitude. The I_0^2 component is two orders of magnitude smaller than I_0^0 . In a corresponding 1D medium the last 4 components of \mathcal{I}^r become zero because of the cylindrical symmetry

of the radiation field. In a 3D medium, these components are non-zero. Specifically for our chosen model the components $I_1^{2,x}$ and $I_1^{2,y}$ are nearly one order of magnitude larger than I_0^2 itself. The components $I_2^{2,x}$ and $I_2^{2,y}$ are of the same order as I_0^2 .

Because I_0^0 is the largest of all the components, the behavior of the \mathcal{I}^r can be understood by considering the action of the first column elements of the $\hat{\Psi}^r$ matrix on I_0^0 . The quantities I_0^0 in panel (a) and I_0^2 in panel (b) are nearly independent of the azimuthal angle φ . This comes from the φ -independence of the elements Ψ_{11}^r and Ψ_{21}^r of the scattering phase matrix in the reduced basis. Ψ_{31}^r and Ψ_{51}^r elements contain $\cos \varphi$ and $\cos 2\varphi$ functions respectively. The φ values are chosen in such a way that $\varphi_i = 2\pi - \varphi_{n_\varphi - i + 1}$ with $i = 1, 2, 3, 4$ and $n_\varphi = 8$. Due to symmetry of $\cos \varphi$ and $\cos 2\varphi$ functions with respect to $\varphi = 2\pi$ and 4π respectively, only 4 curves are distinguishable among the 8 in Figures 4(c) and 4(e). The elements Ψ_{41}^r and Ψ_{61}^r contain $\sin \varphi$ and $\sin 2\varphi$ functions respectively. Due to antisymmetry of $\sin \varphi$ and $\sin 2\varphi$ functions with respect to $\varphi = 2\pi$ and 4π respectively, in Figures 4(d) and 4(f) the curves for φ_i , $i = 1, 2, 3, 4$ have opposite signs with respect to the curves for $\varphi_{n_\varphi - i + 1}$, $n_\varphi = 8$. Moreover, φ_2 and $\pi - \varphi_4$ are close, and φ_5 and $3\pi - \varphi_7$ are also close. Due to symmetry of $\sin \varphi$ with respect to $\varphi = \pi$ and 3π , in Figure 4(d) curves for φ_2 and φ_5 nearly coincide with those for φ_4 and φ_7 respectively. On the other hand, $2\varphi_2$ is close to $2\pi - 2\varphi_4$ and $2\varphi_5$ is close to $6\pi - 2\varphi_7$, which in turn lead to the φ_2 and φ_4 curves and φ_5 and φ_7 curves to have opposite signs in Figure 4(f) due to the anti symmetry of $\sin 2\varphi$ function about $\varphi = 2\pi$ and 6π respectively. Therefore, all the curves are clearly resolved.

In Figure 5 we present the spatially averaged emergent $(I, Q/I, U/I)$ corresponding to the irreducible intensity components shown in Figure 4. The Stokes I profile has dominant contribution from I_0^0 (see Equation (36)). The Q/I profile on the other hand has significant contributions from I_0^2 , $I_1^{2,x}$ and $I_1^{2,y}$. The component I_0^2 is nearly φ -independent, however $I_1^{2,x}$ and $I_1^{2,y}$ are strongly φ -dependent. This dependence is responsible for a strong variation of Q/I with respect to the azimuthal angle φ (see Equation (37)). On the other hand, in a 1D medium I_0^2 is the only component that is responsible for the generation of Stokes Q . Because of this, Q/I in 1D medium becomes φ -

independent. The dominant contribution to U/I comes from $I_1^{2,x}$ and $I_1^{2,y}$. The magnitude of U/I is quite significant, and could become larger than Q/I , unlike the corresponding 1D situation, where $U/I \equiv 0$ always.

5.3. Linear polarization in 3D medium of finite optical depths

In this section we show $(I, Q/I, U/I)$ profiles at chosen spatial points on the top surface ($\tau_Z = 0$). Our purpose is to understand the spatial dependence of the solution. In Figure 6 we show the solutions for a cube defined by $T_X = T_Y = T_Z = T$ with $T = 10$, and 100. All the other model parameters and physical conditions are taken to be the same as in Figure 3. The curves in Figure 6 represent the emergent $(I, Q/I, U/I)$ at the spatial locations marked as points 1–9 on the top surface of the computational cube as shown in Figure 2 (see Table 1 for optical depth information). The corresponding 1D solution is shown for comparison as dash-triple-dotted lines in all the panels.

Stokes I: In Figures 6(a) and 6(d) we plot the Stokes I in 1D and 3D media. The 3D solutions are shown at spatial points 1, 2, 3, 4, 5 as solid, dotted, dashed, dot-dashed, long dashed lines respectively. The results are shown for $\mu = 0.11$ and $\varphi = 7^\circ$. In all the cases, Stokes I shows an emission line spectra, and the $[I]_{3D}$ is less in magnitude than the $[I]_{1D}$. This indicates the leaking in the 3D case, of the radiation through the surface boundaries perpendicular to X and Y directions in contrast to the 1D case characterized by $T_X, T_Y \rightarrow \infty$. As we are showing Stokes I for $\mu = 0.11$ (positive μ direction), the Stokes I for points 2 and 4 are much smaller in magnitude than those at points 3 and 5. This is because the incident intensity is zero at the boundaries adjacent to the points 2 and 4. At points 3 and 5 Stokes I emergent in the direction $\mu = 0.11$ is larger in magnitude due to the contribution of scattering in the medium. Stokes I shows a larger spatial gradient in the regions covered by $[T_X, T_X/2]$ and $[T_Y, T_Y/2]$, when compared to the region covered by $[T_X/2, 0]$ and $[T_Y/2, 0]$. This can be seen clearly by looking at the surface plots, namely Figure 7(a) and 7(b).

Stokes Q: In Figures 6(b) and 6(e) we plot the

Q/I in 1D and 3D medium. The 3D solutions are shown at spatial points 1, 2, 3, 6, 7 as solid, dotted, dashed, dot-dashed, long dashed lines respectively. There exist significant differences between $[Q/I]_{1D}$ and $[Q/I]_{3D}$. For $T = 10$, the maximum value of $[[Q/I]]_{3D}$ is for the spatial location 2. At this point, $[[Q/I]]_{3D}$ is about 4 percent and $[[Q/I]]_{1D}$ is 3 percent at line center. However in the near wings ($x \leq 6$), $[[Q/I]]_{1D}$ reaches a maximum of around 8 percent at $x = 2$ and the corresponding $[[Q/I]]_{3D}$ is around 3 percent. For $T = 100$, the $[[Q/I]]_{3D}$ reaches a maximum of 10 percent for the spatial point 2 at $x = 2$ and $[[Q/I]]_{1D}$ reaches maximum of 7 percent at $x = 4$. For the points 2 and 6, $[[Q/I]]_{3D}$ takes largest values for both $T = 10$ and $T = 100$. The dominant quantity that dictates the emergent Q/I is the radiation anisotropy within the cube. The above results show the existence of a sharp variation of anisotropy within the cube than within a slab which has only one degree of freedom for transfer in the spatial domain. Also from the surface plots Figures 7(c) and 7(d) we see a sharp variation of $[[Q/I]]_{3D}$ at the edges of the top surface. However, the polarization remains nearly constant (≈ 2 percent) at $x = 0$ in the inner parts of the top surface. The spatial variation of $[[Q/I]]_{3D}$ at $x = 2$ is quite different from that at $x = 0$. There is a sharp increase in $[[Q/I]]_{3D}$ near the edge region ($\tau_X = 0$ or $\tau_X = T_X$), reaching a maximum value of around 10 percent.

Stokes U: In Figures 6(c) and 6(f) we show U/I in 1D and 3D medium. The 3D solutions are shown at spatial points 1, 4, 5, 6, 7 as solid, dotted, dashed, dot-dashed, long dashed lines respectively. $[[U/I]]_{1D} \equiv 0$, whereas $[[U/I]]_{3D}$ has a significant value. The variation of $[[U/I]]_{3D}$ with an increase in T is analogous to the behavior of $[[Q/I]]_{3D}$. For the points 4 and 5, $[[U/I]]_{3D}$ takes largest values for both $T = 10$ and $T = 100$. It reaches a maximum of 15 percent at the spatial point 4, for $x = 0$ and $T=10$ (see Figure 6(c)) and 25 percent at the spatial point 4, for $x = 2$ and $T=100$ (see Figure 6(f)). This shows that U/I is much more sensitive to the anisotropy of the radiation field within a 3D medium. At the spatial point 1, $[[U/I]]_{3D} \approx 0$ as expected, namely the axisymmetry of the emergent radiation at the central point. From the surface plots Figures 7(e) and 7(f) we can see a large variation of $[[U/I]]_{3D}$ again

at the edges of the cube, where non-axisymmetry reaches maximum. As in $[[Q/I]]_{3D}$ the behavior of $[[U/I]]_{3D}$ at $x = 2$ is quite different from that at $x = 0$. However its maximum is now reached near the edge region ($\tau_Y = 0$ or $\tau_Y = T_Y$), which is oriented at 90° with respect to the regions where $[[Q/I]]_{3D}$ shows a maximum variation ($\tau_X = 0$ or $\tau_X = T_X$). In general, the run of anisotropy in the 3D case depends on the optical depths in X , Y and Z directions simultaneously. This is clearly seen in the complicated frequency dependence of $(Q/I, U/I)$ profiles in the 3D case unlike the 1D case. Although the linear polarization $(Q/I, U/I)$ may take large values at different spatial points (for e.g., points 1–9), the surface averaged values of $(Q/I, U/I)$ are usually less, in the self-emitting cubes that we have considered in this paper. The effect of surface averaging can be seen in Figure 5. The fact that 1D values of $(Q/I, U/I)$ differ considerably from the 3D situation shows that realistic modeling of the observed linear polarization using 3D model atmospheres is not as straight forward as the use of 1D model atmospheres.

5.4. The effect of collisional redistribution on the Stokes parameters in a 3D medium

Figure 8 shows spatially averaged $(I, Q/I, U/I)^T$ results computed for a $T = 100$ model with a range of elastic collision rate parameters $\Gamma_E/\Gamma_R = (10^{-4}, 0.1, 1, 10)$. The models corresponding to the curves shown in Figure 8 are given in Table 2. Models 2 and 3 can be termed as radiative de-excitation models (dominated by R_{II} -type PRD). Model 4 has a mixture of R_{II} and R_{III} type PRD scattering mechanisms. The collisions dominate (R_{III} -type PRD) in the model 5. Model 1, corresponding to CRD, is presented for comparisons.

Stokes I: The Stokes I is controlled by α and $\beta^{(0)} - \alpha$. The line core ($x \leq 1$) of the Stokes I profile is unaffected by collisions. In the line core, the R_{II} and R_{III} type functions both behave like CRD function, and hence the PRD and CRD profiles are similar. As we go from models 2 to 5, the relative contribution of R_{III} progressively increases throughout the line profile. However its effect is felt only in the wings ($x \geq 2$).

Stokes Q: The ratio Q/I is controlled by α and

$\beta^{(2)} - \alpha$. The models 1 to 3 yield nearly the same magnitude for $[[Q/I]]_{3D}$ at line center again because of the CRD-type behavior of R_{II} and R_{III} in the line core. In model 4, both R_{II} and R_{III} are weighted by smaller values of α and $\beta^{(2)} - \alpha$. This causes a large depolarization in the line core. In the near line wings, R_{II} dominated models 2 and 3 show largest polarization (≈ 1.5 percent). In the CRD case (model 1), the scattering integral becomes constant in the optically thin wings. This is because the contribution of the wing frequencies to the scattering integral becomes smaller and smaller, in comparison to the contribution from the core frequencies. For this reason, the anisotropy and hence the wing polarization takes a constant value. In models 2 and 3 R_{II} type scattering dominates throughout the profile. For these cases, the scattering integral approaches zero and hence only the thermal (isotropic) part contributes to the line source function. As a consequence, polarization goes to zero in these optically thin wings (see Faurobert 1987). The other two models are a combination of these two extreme conditions and therefore the corresponding Q/I curves lie in between the two extreme situations.

Stokes U: As discussed before, generation of Stokes U is a characteristic of multi-D transfer (through a large non-axisymmetry). The qualitative behavior of U/I profile is similar to that of Q/I for all the models. In the CRD case the magnitude of U/I in the wings is much larger (≈ 2 percent) than that of Q/I (≈ 0.72 percent).

6. Conclusions

In this paper we formulate the polarized transfer equation in 3D geometry using the technique of irreducible spherical tensors $\mathcal{T}_Q^K(i, \Omega)$. The polarized transfer equation for the irreducible components of the Stokes parameters lends itself for solution by the standard PALI methods, extended appropriately to handle the transfer of the rays in a 3D geometry. We present 3D solution on some test cases, which may serve as benchmarks. The nature of line radiative transfer in 3D geometry, as compared to the 1D case is discussed in some detail.

We show that the 3D PALI method gives correct results in the limit of 1D geometry. The

3D transfer is characterized by the anisotropy of the radiation field within the computational cube. The 3D anisotropy is characteristically different from the 1D anisotropy of the radiation field. The difference arises due to the finite optical depths in the horizontal directions (X, Y). This causes large differences between the 3D and 1D values of the degree of linear polarization ($Q/I, U/I$). In fact, in 3D geometry the radiation field is non-axisymmetric (even in the absence of magnetic fields) because the finite optical depths in X, Y, Z directions break the azimuthal symmetry of the radiation field. In a 1D geometry, the radiation field is axisymmetric about the Z -axis. Due to these reasons, the shapes and magnitude of the $(Q/I, U/I)$ spectra differ significantly from the corresponding 1D cases. We compare the surface averaged $(I, Q/I, U/I)$ spectra computed under the CRD and PRD assumptions. The nature of differences between CRD and PRD profiles in 3D geometry remain the same as that for the 1D geometry. We notice that $[[U/I]]_{3D}$ is in general larger in magnitude, than $[[Q/I]]_{3D}$ in the 3D models. This is because the radiation field in a 3D medium is highly non-axisymmetrical in nature. The degree of linear polarization in the spatially resolved $(Q/I, U/I)$ spectra are generally larger in magnitude when compared to the corresponding surface averaged values, clearly due to the fact that a surface averaging over sign changing quantities leads to smaller values of Q/I and U/I . Another reason for this is the fact that linear polarization is largest in the very narrow regions close to the boundaries (see Figure 7). When a surface averaging is performed, the relative contributions from these highly polarized narrow regions are dominated over by the inner regions, where the linear polarization is considerably smaller.

We show that the advantage of solving the transfer equation in the irreducible components basis, is that the irreducible source vector S_Q^K becomes completely independent of the angle variables, making it easier to extend the existing 1D PALI methods to the 3D case. However the irreducible intensity components I_Q^K remain dependent on the inclination and also on the azimuthal angle of the ray. It is important to recognize the fact that the multipolar expansion for Stokes intensity and Stokes source vectors presented in this paper allows us to write a transfer equation in

terms of I_Q^K and S_Q^K . A further advantage is that this formalism allows to efficiently use the scattering phase matrix approach to different problems in multi-D geometry. We have demonstrated this by taking the example of polarized line transfer with PRD. In the following papers we try to apply the solution method presented in this paper, to model the polarimetric observations of the resolved structures like solar filaments and prominences.

Acknowledgments: We would like to thank Johannes Adam for providing a copy of his 3D unpolarized transfer code which is adapted in this paper to compute the formal solution. We are grateful to Prof. H. Frisch for critical reading of the manuscript and useful suggestions which helped to improve the paper substantially. We thank Dr. M. Sampoorna for helpful comments and suggestions. We thank Dr. M. Bianda for useful discussions.

A. The scattering phase matrix in real form in the reduced basis

In § 3.2 it was mentioned that for practical computations, it is preferable to work with the real form of the scattering phase matrix, in the reduced basis. Here we list the elements of such a 6×6 phase matrix. The coefficients $\mathcal{T}_Q^K(i, \mathbf{\Omega})$ depend on a reference angle, usually denoted by γ , to define the reference frame of the electric field in a plane perpendicular to $\mathbf{\Omega}$. Here we take $\gamma = 0$, which means that positive Q is defined to be in a direction perpendicular to the surface ($\tau_Z = 0$). The phase matrix is written as

$$\hat{\Psi}^r = \begin{pmatrix} \Psi_{11}^r & \Psi_{12}^r & \Psi_{13}^r & \Psi_{14}^r & \Psi_{15}^r & \Psi_{16}^r \\ \frac{1}{2}\Psi_{12}^r & \Psi_{22}^r & \Psi_{23}^r & \Psi_{24}^r & \Psi_{25}^r & \Psi_{26}^r \\ \frac{1}{2}\Psi_{13}^r & \frac{1}{2}\Psi_{23}^r & \Psi_{33}^r & \Psi_{34}^r & \Psi_{35}^r & \Psi_{36}^r \\ \frac{1}{2}\Psi_{14}^r & \frac{1}{2}\Psi_{24}^r & \Psi_{34}^r & \Psi_{44}^r & \Psi_{45}^r & \Psi_{46}^r \\ \frac{1}{2}\Psi_{15}^r & \frac{1}{2}\Psi_{25}^r & \Psi_{35}^r & \Psi_{45}^r & \Psi_{55}^r & \Psi_{56}^r \\ \frac{1}{2}\Psi_{16}^r & \frac{1}{2}\Psi_{26}^r & \Psi_{36}^r & \Psi_{46}^r & \Psi_{56}^r & \Psi_{66}^r \end{pmatrix}, \quad (\text{A1})$$

where the distinct matrix elements are:

$$\begin{aligned} \Psi_{11}^r &= 1; & \Psi_{12}^r &= \frac{1}{2\sqrt{2}}(3\cos^2\theta - 1); \\ \Psi_{13}^r &= -\frac{\sqrt{3}}{2}\sin 2\theta \cos \varphi; & \Psi_{14}^r &= \frac{\sqrt{3}}{2}\sin 2\theta \sin \varphi; & \Psi_{15}^r &= \frac{\sqrt{3}}{2}\sin^2\theta \cos 2\varphi; \\ \Psi_{16}^r &= -\frac{\sqrt{3}}{2}\sin^2\theta \sin 2\varphi; & \Psi_{22}^r &= \frac{1}{4}(9\cos^4\theta - 12\cos^2\theta + 5); \\ \Psi_{23}^r &= \frac{\sqrt{3}}{4\sqrt{2}}\sin 2\theta(1 - 3\cos 2\theta)\cos \varphi; & \Psi_{24}^r &= -\frac{\sqrt{3}}{4\sqrt{2}}\sin 2\theta(1 - 3\cos 2\theta)\sin \varphi; \\ \Psi_{25}^r &= \frac{\sqrt{3}}{2\sqrt{2}}\sin^2\theta(1 + \cos^2\theta)\cos 2\varphi; & \Psi_{26}^r &= -\frac{\sqrt{3}}{2\sqrt{2}}\sin^2\theta(1 + \cos^2\theta)\sin 2\varphi; \\ \Psi_{33}^r &= \frac{3}{4}\sin^2\theta[(1 + 2\cos 2\theta) - (1 - 2\cos 2\theta)\cos 2\varphi]; \\ \Psi_{34}^r &= \frac{3}{4}\sin^2\theta(1 - 2\cos 2\theta)\sin 2\varphi; & \Psi_{35}^r &= \frac{3}{16}\sin^2\theta[(3 + \cos 2\theta)\sin \varphi - (1 - 2\cos 2\theta)\sin 3\varphi]; \\ \Psi_{36}^r &= -\frac{3}{16}\sin^2\theta[(3 + \cos 2\theta)\sin \varphi - (1 - 2\cos 2\theta)\sin 3\varphi]; \\ \Psi_{44}^r &= \frac{3}{4}\sin^2\theta[(1 + 2\cos 2\theta) + (1 - 2\cos 2\theta)\cos 2\varphi]; \\ \Psi_{45}^r &= \frac{3}{16}\sin^2\theta[(3 + \cos 2\theta)\sin \varphi + (1 - 2\cos 2\theta)\sin 3\varphi]; \\ \Psi_{46}^r &= \frac{3}{16}\sin^2\theta[(3 + \cos 2\theta)\cos \varphi + (1 - 2\cos 2\theta)\cos 3\varphi]; \\ \Psi_{55}^r &= \frac{3}{16}[(1 + 6\cos^2\theta + \sin^4\theta + \cos^4\theta) + (1 - 2\cos^2\theta + \cos^4\theta + \sin^4\theta)\cos 4\varphi]; \\ \Psi_{56}^r &= -\frac{3}{16}[(1 - 2\cos^2\theta + \cos^4\theta + \sin^4\theta)\sin 4\varphi]; \\ \Psi_{66}^r &= \frac{3}{16}[(1 + 6\cos^2\theta + \sin^4\theta + \cos^4\theta) - (1 - 2\cos^2\theta + \cos^4\theta + \sin^4\theta)\cos 4\varphi]. \end{aligned} \quad (\text{A2})$$

The elements of the matrix $\hat{\Psi}^r$ satisfy certain symmetry properties with respect to the main diagonal. Hence the number of independent elements are only 21.

B. A core-wing method for the 3D polarized line transfer

An unpolarized version of the core-wing method was originally developed by Paletou & Auer (1995). It was extended later to resonance polarization with PRD by Paletou & Faurobert-Scholl (1997) and to the Hanle effect by Nagendra et al. (1999). The above cited papers used simple forms of PRD functions (combination of $R_{II, III}$ of Hummer 1962). Fluri et al. (2003) proposed a core-wing method for the Hanle scattering problem with the very general PRD matrices of Bommier (1997).

The core-wing method assumes that CRD is a good description in the line core region ($x \leq x_c$) and frequency coherent scattering (CS) is a good approximation in the line wings ($x > x_c$). The choice of the separation frequency x_c is not critical. A practical choice is $x_c = 3.5$. In other words the R_{II} function of Hummer (1962) can be replaced by a weighted combination of CRD and CS. R_{III} function is set to CRD in the line core, and to zero in the line wings.

The application of the core-wing separation method to Equation (43) leads to

$$\begin{aligned} \int_{-\infty}^{+\infty} dx' \frac{\hat{R}(x, x')}{\phi(x)} \hat{\Lambda}_{x'}^* p_{x'} \delta \mathcal{S}_l^{r, n}(\mathbf{r}, x') &= (1 - g_x) \int_{core} dx' \hat{W} [\hat{\alpha} \phi(x') + (\hat{\beta} - \hat{\alpha}) \phi(x')] \hat{\Lambda}_{x'}^* p_{x'} \delta \mathcal{S}_l^{r, n}(\mathbf{r}, x') \\ + g_x \int_{wing} dx' \hat{W} \hat{\alpha} \frac{\delta(x - x') \phi(x')}{\phi(x)} \hat{\Lambda}_{x'}^* p_{x'} \delta \mathcal{S}_l^{r, n}(\mathbf{r}, x'), \end{aligned} \quad (B1)$$

where

$$g_x = \begin{cases} 0 & \text{for } x \leq x_c, \\ \frac{R_{III}(x, x)}{\phi(x)} & \text{for } x > x_c, \end{cases} \quad (B2)$$

is the separation coefficient. Simplifying the above integral we obtain

$$\begin{aligned} \delta \overline{\mathcal{J}}^{r, n}(\mathbf{r}, x) &= \int_{core} dx' \hat{W} \hat{\beta} \phi(x') \hat{\Lambda}_{x'}^* p_{x'} \delta \mathcal{S}_l^{r, n}(\mathbf{r}, x') \quad \text{for } x \leq x_c, \\ \text{and} \\ \delta \overline{\mathcal{J}}^{r, n}(\mathbf{r}, x) &= (1 - g_x) \int_{core} dx' \hat{W} \hat{\beta} \phi(x') \hat{\Lambda}_{x'}^* p_{x'} \delta \mathcal{S}_l^{r, n}(\mathbf{r}, x') + g_x \hat{W} \hat{\alpha} \hat{\Lambda}_x^* p_x \delta \mathcal{S}_l^{r, n}(\mathbf{r}, x) \quad \text{for } x > x_c. \end{aligned} \quad (B3)$$

Substituting Equation (B3) in Equation (43) we obtain separate equations for $\overline{\mathcal{J}}^{r, n+1}(\mathbf{r}, x)$ in the core and the wing domains. After simple algebraic manipulations, Equation (44) can be re-written as

$$\delta \mathcal{S}_l^{r, n}(\mathbf{r}, x) = \delta \overline{\mathcal{J}}^{r, n}(\mathbf{r}, x) + \mathbf{r}_x^n, \quad (B4)$$

where $\delta \overline{\mathcal{J}}^{r, n}$ is given by Equation (B3). The residual vector \mathbf{r}_x^n is

$$\mathbf{r}_x^n = \overline{\mathcal{J}}^{r, n}(\mathbf{r}, x) + \epsilon \mathbf{B}(\mathbf{r}) - \mathcal{S}_l^{r, n}(\mathbf{r}, x). \quad (B5)$$

We now proceed to derive the line source vector corrections for the core domain. Defining a vector

$$\Delta \mathbf{T}^n = \int_{core} dx' \hat{W} \hat{\beta} \phi(x') \hat{\Lambda}_{x'}^* p_{x'} \delta \mathcal{S}_l^{r, n}(\mathbf{r}, x'), \quad (B6)$$

the line source vector correction takes the form

$$\delta \mathcal{S}_l^{r, n}(\mathbf{r}, x) = \mathbf{r}_x^n + \Delta \mathbf{T}^n, \quad \text{for } x \leq x_c. \quad (B7)$$

Applying the integral operator $\int_{core} dx' \hat{W} \hat{\beta} \phi(x') p_{x'} \hat{\Lambda}_x^*$, on both sides of the Equation (B7), we finally obtain

$$\Delta \mathbf{T}^n = \frac{\overline{\mathbf{r}}^n}{1 - \int_{core} dx' \hat{W} \hat{\beta} \phi(x') p_{x'} \hat{\Lambda}_x^*}, \quad (B8)$$

where

$$\bar{\mathbf{r}}^n = \int_{core} dx' \hat{W} \hat{\beta} \phi(x') p_{x'} \hat{\Lambda}_{x'}^* \mathbf{r}_{x'}^n. \quad (\text{B9})$$

Notice that $\bar{\mathbf{r}}^n$ and $\Delta \mathbf{T}^n$ are independent of the frequency x . Using Equations (43), (B3) and (B7) we obtain

$$\delta \mathcal{S}_l^{r,n}(\mathbf{r}, x) = \frac{(1 - g_x) \Delta \mathbf{T}^n + \mathbf{r}_x^n}{[1 - g_x \hat{W} \alpha \hat{\Lambda}_x^* p_x]}, \quad \text{for } x > x_c. \quad (\text{B10})$$

The updated line source vector can be computed using

$$\mathcal{S}_l^{r,n+1}(\mathbf{r}, x) = \mathcal{S}_l^{r,n}(\mathbf{r}, x) + \delta \mathcal{S}_l^{r,n}(\mathbf{r}, x). \quad (\text{B11})$$

The above core-wing equations are set up in the form of an iterative algorithm to compute the line source vector corrections. We define

$$c_1 = \max_{\tau_X, \tau_Y, \tau_Z, x} \left\{ \frac{\delta \mathcal{S}_{0,l}^{0,r,n}(\mathbf{r}, x)}{\mathcal{S}_{0,l}^{0,r,n}(\mathbf{r}, x)} \right\}, \quad \text{and} \quad p = \max_{\tau_X, \tau_Y} \left\{ \frac{1}{I} \sqrt{Q^2 + U^2} \right\}, \quad (\text{B12})$$

where the I , Q and U are computed at the top surface ($\tau_Z = 0$). Further, we consider p only at the line center ($x = 0$), and for $\mu = 0.11$, and $\varphi = 7^\circ$. Finally we define the maximum relative change (MRC) as

$$R_c^n = \max \{c_1, p\}. \quad (\text{B13})$$

The iterative progress is followed through a convergence test on R_c^n . We have chosen a convergence criteria of 10^{-4} on the R_c^n .

REFERENCES

- Adam, J. 1990, *A&A*, 240, 541
- Auer, L. H., & Paletou, F. 1994, *A&A*, 285, 675
- Auer, L. H., Fabiani Bendicho, P., & Trujillo Bueno, J. 1994, *A&A*, 292, 599
- Bommier, V. 1997, *A&A*, 328, 726
- Chandrasekhar, S. 1960, *Radiative Transfer* (New York: Dover)
- Dittmann, O. J. 1997, *JQSRT*, 57, 249
- Dittmann, O. J. 1999, in *Solar Polarization*, ed. K. N. Nagendra & J. O. Stenflo (Boston: Kluwer), 201
- Domke, H., & Hubeny, I. 1988, *ApJ*, 334, 527
- Dumont, S., Pecker, J. C., Omont, A., & Rees, D. 1977, *A&A*, 54, 675
- Faurobert, M. 1987, *A&A*, 178, 269
- Faurobert-Scholl, M. 1991, *A&A*, 246, 469
- Faurobert-Scholl, M., 1992, *A&A*, 258, 521
- Fluri, D. M., Nagendra, K. N., & Frisch, H. 2003, *A&A*, 400, 303
- Folini, D., 1998 PhD Thesis, ETH No. 12606, ETH Zurich
- Frisch, H. 2007, *A&A*, 476, 665 (HF07)
- Frisch, H., Anusha, L. S., Sampoorana, M., & Nagendra, K. N. 2009, *A&A*, 501, 335
- Hillier, D. J. 1996, *A&A*, 308, 521
- Hummer, D. G. 1962, *MNRAS*, 125, 21
- Jeffrey, D. J. 1989, *ApJ Suppl. Ser.* 71, 951
- Kunasz, P., & Auer, L. H. 1988, *JQSRT*, 39, 67
- Landi Degl'Innocenti, E., & Landolfi, M. 2004, *Polarization in Spectral Lines* (Dordrecht: Kluwer) (LL04)
- Manso Sainz, R., & Trujillo Bueno, J. 1999, in *Solar Polarization*, ed. K. N. Nagendra & J. O. Stenflo (Boston: Kluwer), 143
- Mihalas, D., Auer, L. H., & Mihalas, B. R. 1978, *ApJ*, 220, 1001
- Nagendra, K. N. 1988, *ApJ*, 335, 269
- Nagendra, K. N. 1994, *ApJ*, 432, 274
- Nagendra, K. N., Frisch, H., & Faurobert-Scholl, M. 1998, *A&A*, 332, 610
- Nagendra, K. N., Paletou, F., Frisch, H., & Faurobert-Scholl, M. 1999, in *Solar Polarization*, ed. K. N. Nagendra & J. O. Stenflo (Boston: Kluwer), 127
- Nagendra, K. N., Frisch, H., & Faurobert, M. 2002, *A&A*, 395, 305
- Nagendra, K. N., Bonifacio, P., & Ludwig, H.-G., eds. 2009, *3D views on cool stellar atmospheres: theory meets observation*, *Memoire della Societe Astronomica Italiana*, 80
- Paletou, F., & Auer, L. H. 1995, *A&A*, 297, 771
- Paletou, F., Bommier, V., & Faurobert-Scholl, M. 1999, in *Solar Polarization*, ed. K. N. Nagendra & J. O. Stenflo (Boston: Kluwer), 189
- Paletou, F., & Faurobert-Scholl, M. 1997, *A&A*, 328, 343
- Papkalla, R. 1995, *A&A*, 295, 551
- Rees, D. E., & Saliba, G. J. 1982, *A&A*, 115, 1
- Sampoorna, M., Nagendra, K. N., & Stenflo, J. O. 2008a, *ApJ*, 679, 889
- Sampoorna, M., Nagendra, K. N., & Frisch, H. 2008b, *JQSRT*, 109, 2349
- Sampoorna, M., & Trujillo Bueno, J. 2010, *ApJ*, 712, 1331
- Stenflo, J. O. 1976, *A&A*, 46, 61
- Stenflo, J. O. 1994, *Solar Magnetic Fields: Polarized Radiation Diagnostics* (Dordrecht: Kluwer)
- Trujillo Bueno, J., & Shchukina, N. 2007, *ApJ*, 664, 135
- Trujillo Bueno, J., & Shchukina, N. 2009, *ApJ*, 694, 1364

Trujillo Bueno, J., Shchukina, N., & Asensio
Ramos, A. 2004, *Natur.* 430, 326

van Noort, M., Hubeny, I., & Lanz, T. 2002, *ApJ*,
568, 1066

Vath, H. M. 1994, *A&A*, 284, 319

Table 1: The optical depth information for the spatial points 1–9 on the top surface ($\tau_Z = 0$) in Figure 2.

Spatial point	τ_X	τ_Y	τ_Z
1	$T_X/2$	$T_Y/2$	0
2	T_X	$T_Y/2$	0
3	0	$T_Y/2$	0
4	$T_X/2$	T_Y	0
5	$T_X/2$	0	0
6	0	T_Y	0
7	T_X	0	0
8	0	0	0
9	T_X	T_Y	0

Table 2: The values of the free parameters corresponding to different models shown in Figure 8.

Model	Scat. mechanism	α	$\beta^{(0)}$	$\beta^{(2)}$	$(\beta^{(0)} - \alpha)$	$(\beta^{(2)} - \alpha)$
1	CRD	0.00	1.00	1.00	1.00	1.00
2	$\Gamma_E/\Gamma_R = 10^{-4}$	0.99	0.99	0.99	0.00	0.00
3	$\Gamma_E/\Gamma_R = 0.1$	0.90	0.99	0.96	0.09	0.06
4	$\Gamma_E/\Gamma_R = 1$	0.49	0.99	0.72	0.50	0.23
5	$\Gamma_E/\Gamma_R = 10$	0.09	0.99	0.21	0.89	0.12

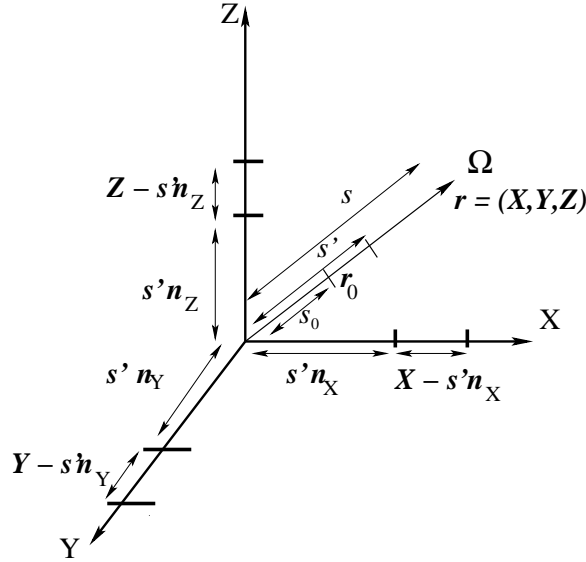


Fig. 1.— The definition of the spatial location \mathbf{r} and the projected distances $\mathbf{r} - s'\mathbf{\Omega}$ which appear in the 3D formal solution integral. \mathbf{r}_0 and \mathbf{r} are the arbitrary initial and final locations considered in the formal solution integral.

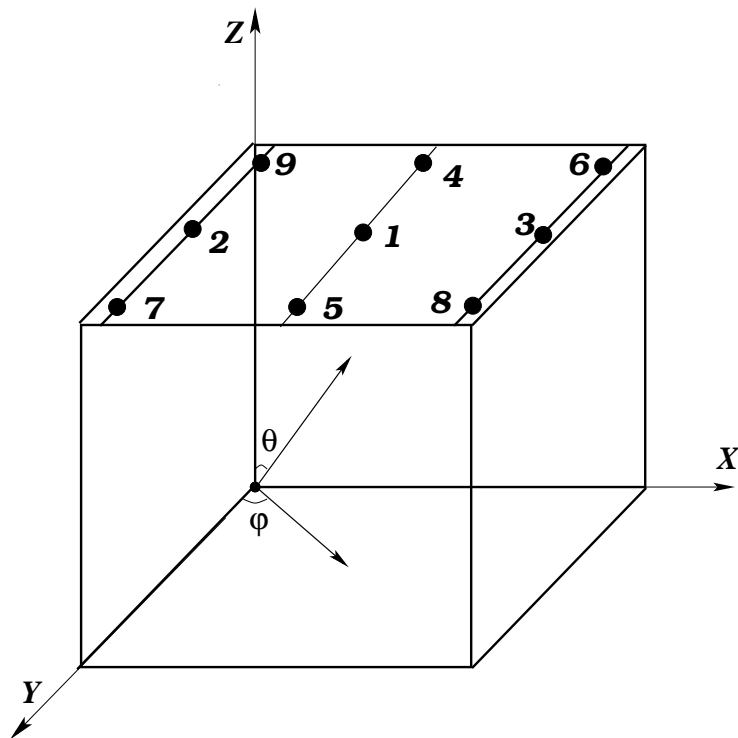


Fig. 2.— The geometry of the problem. The angle pair (θ, φ) defines the ray direction. The optical depth information of the spatial points 1–9 on the top surface ($\tau_Z = 0$) of the computational cube are given in Table 1. The results are shown at the points marked on grid lines which are just inside the outermost boundaries. The Z axis is along the atmospheric normal.

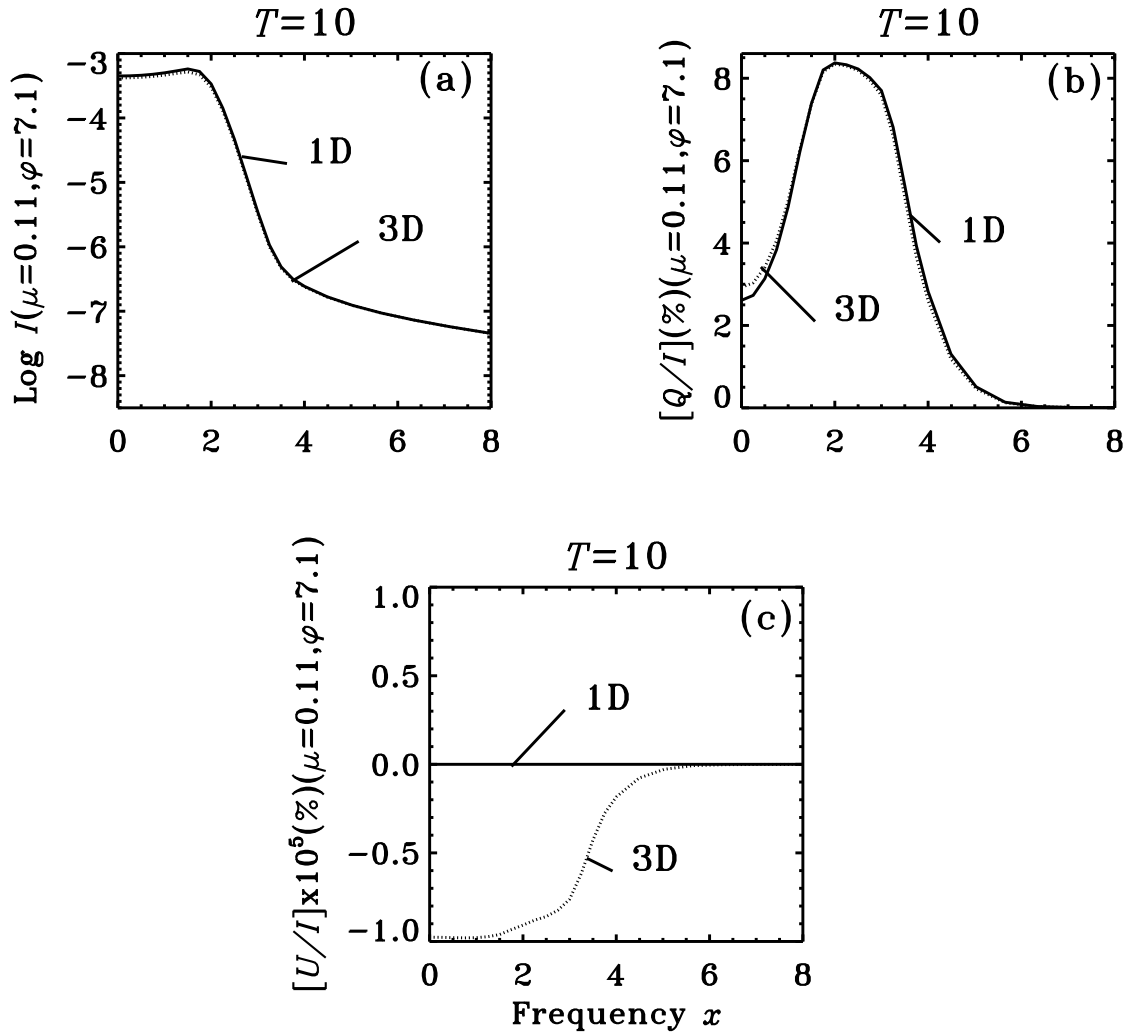


Fig. 3.— Validation of a 3D radiative transfer solution through a comparison with a 1D benchmark. The dotted line represents the solution for a 3D medium that mimics 1D planar slab of optical thickness $T = 10$. The solid line is the 1D solution. The model parameters chosen for the 3D cube are given in § 5.1.

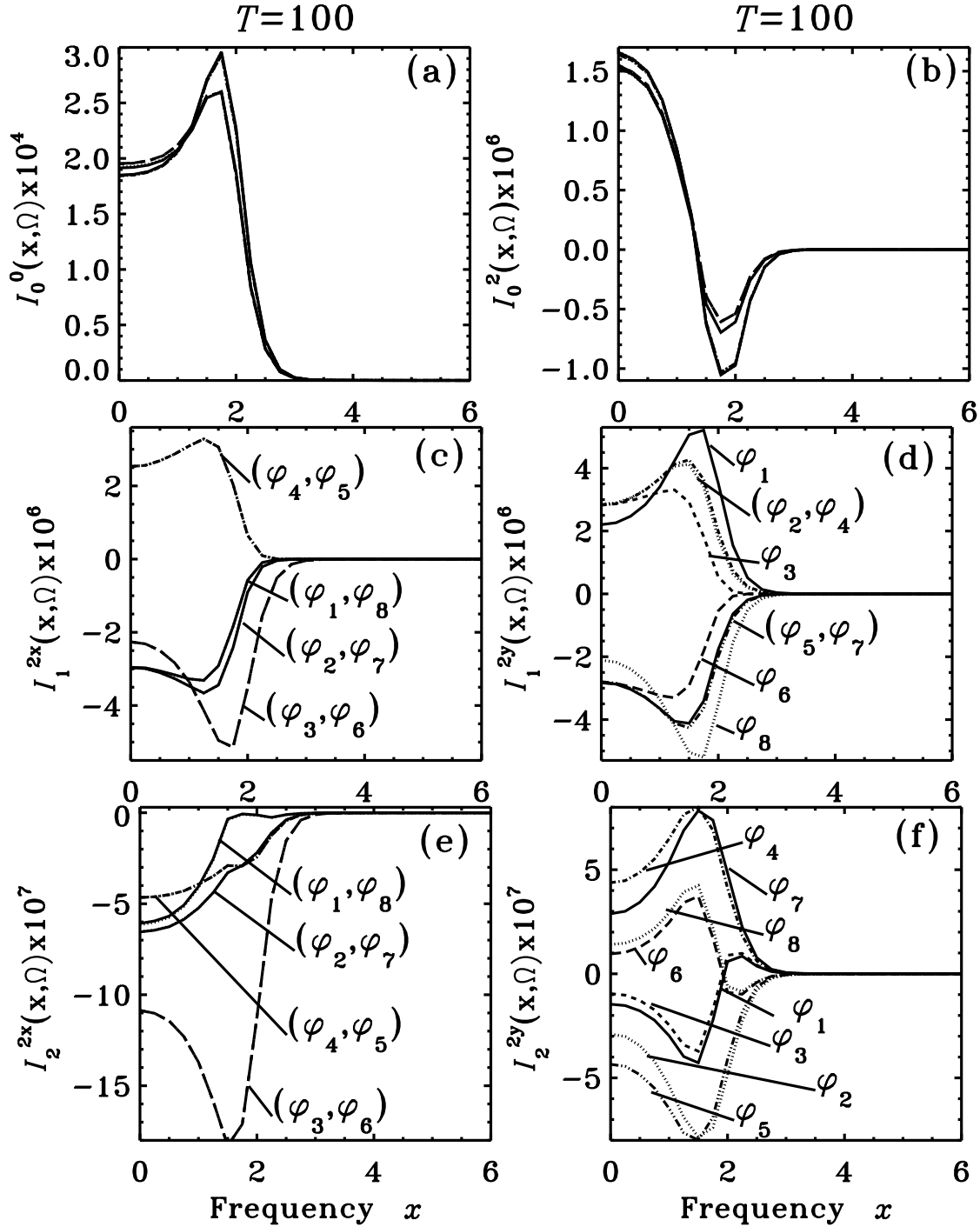


Fig. 4.— The azimuth angle (φ) dependence of the surface averaged irreducible intensity components of polarization at $\tau_Z = 0$ in a 3D medium. The model parameters used are the same as those in Figure 3 except for $T_X=T_Y=T_Z=T=100$. The values of the azimuth are $\varphi_{1,8}=7^\circ, 36^\circ, 85^\circ, 146^\circ, 213^\circ, 274^\circ, 323^\circ, 352^\circ$. The intensity components approach a constant small value, or tend to zero in the wings ($x \geq 3$).

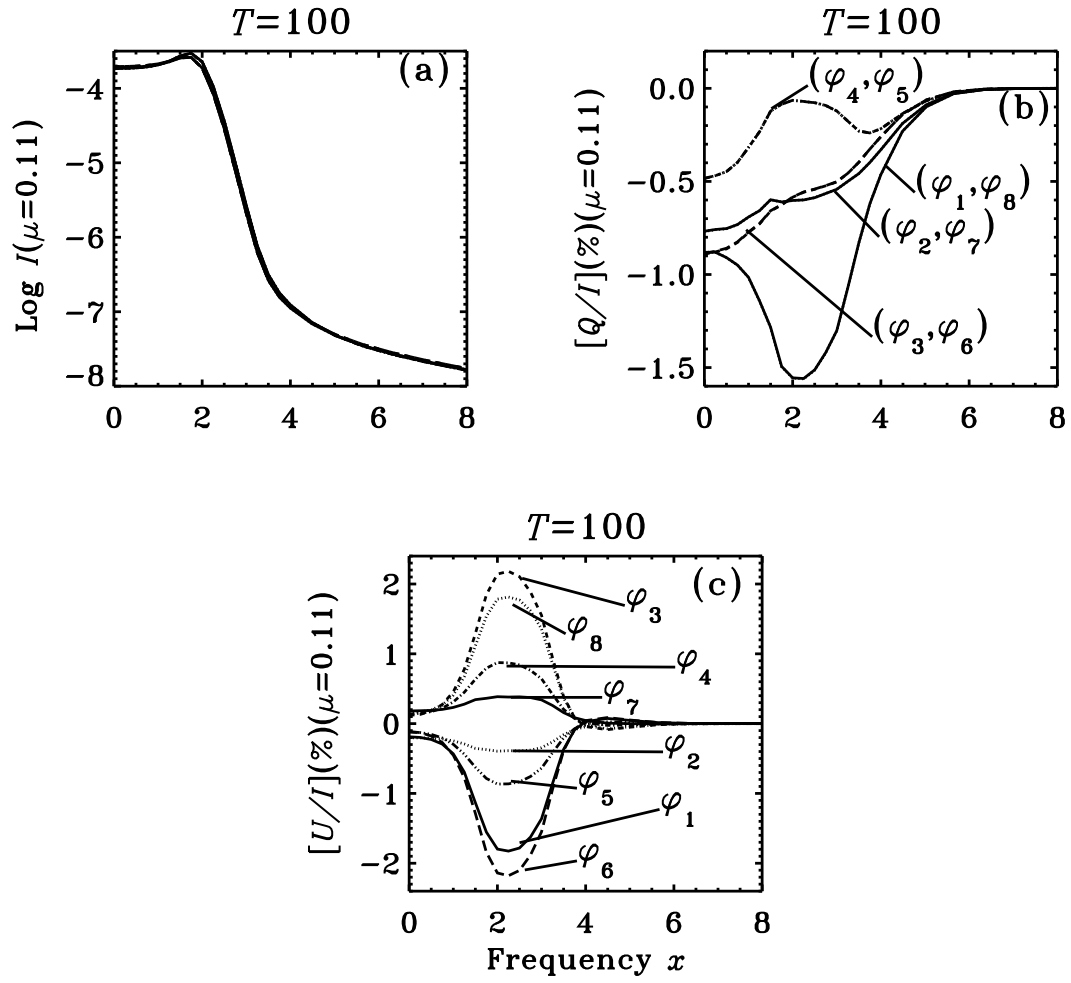
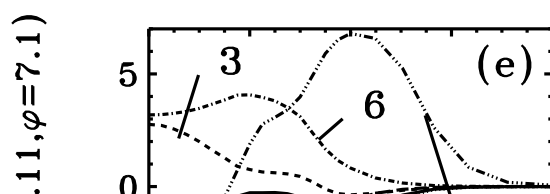
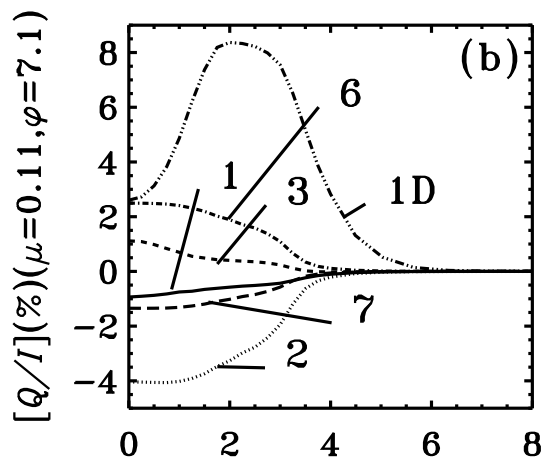
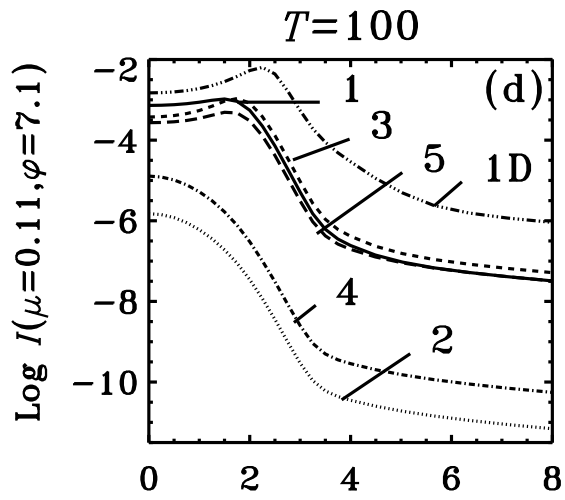
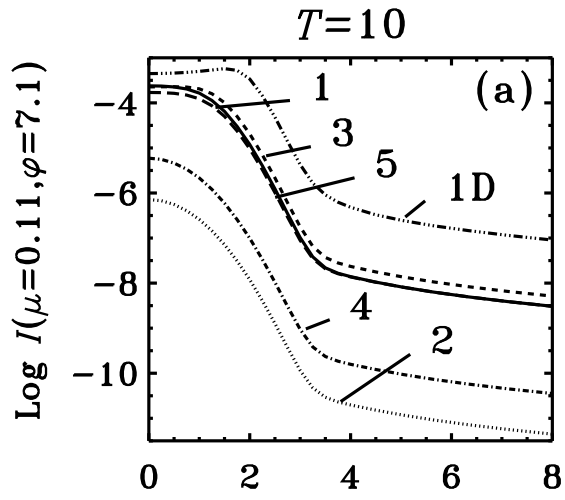


Fig. 5.— Spatially averaged emergent ($I, Q/I, U/I$) in a 3D medium. The model parameters are the same as those in Figure 4.



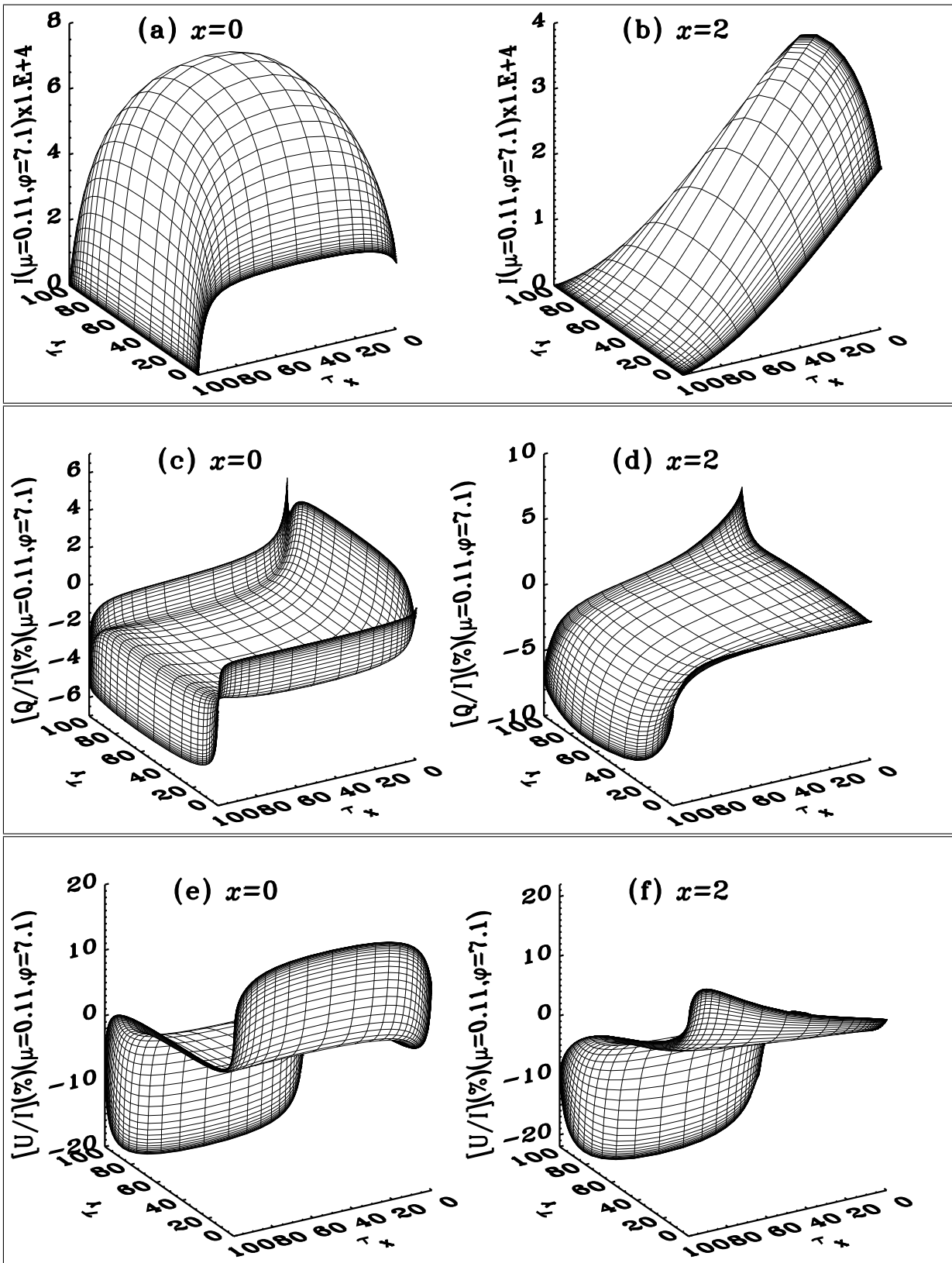


Fig. 7.— Surface plots of the intensity I and the degree of linear polarization ($Q/I, U/I$) on the top surface ($\tau_z = 0$) of the computational cube. The model parameters are same as in the $T = 100$ case of Figure 6. See § 5.3 for details.

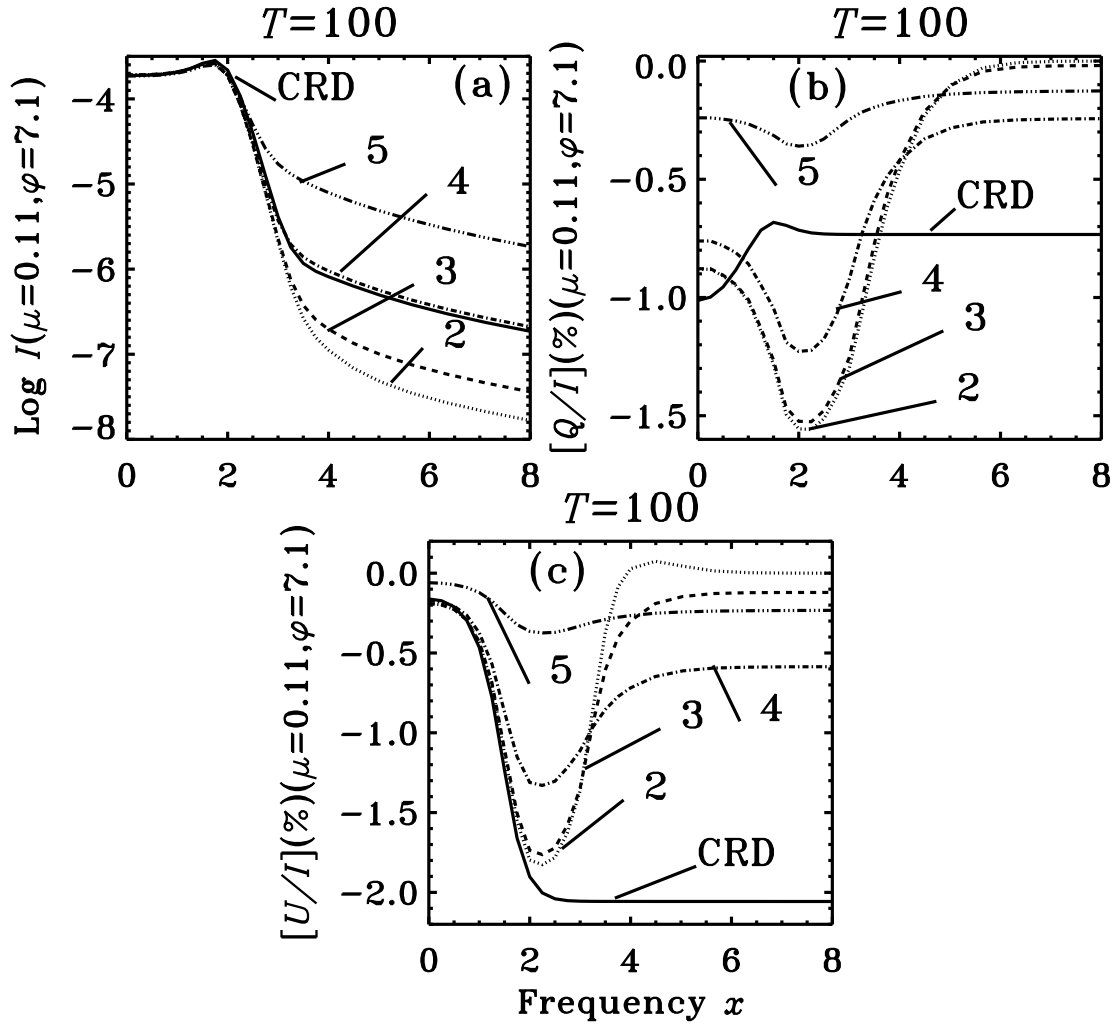


Fig. 8.— The effect of collisions on the surface averaged emergent ($I, Q/I, U/I$). The model parameters are the same as in Figure 5. Refer to Table 2 for details of the branching ratios. The solid lines represent the special case of CRD solution. The indices near the curves correspond to the model numbers given in Table 2. The collisions have a strong effect on polarization in a 3D geometry (which has a non-zero U/I), as in the case of a 1D slab.